New Journal of Physics
An Institute of Physics and Deutsche Physikalische Gesellschaft Journal

Large-scale fluctuation structures in plasma turbulence

O Grulke and T Klinger
Max-Planck-Institute for Plasma Physics, Greifswald Branch,
EURATOM Association, D-17491 Greifswald, Germany
and
Ernst-Moritz-Arndt University, D-17489 Greifswald, Germany
E-mail: grulke@ipp.mpg.de

New Journal of Physics **4** (2002) 67.1–67.23 (http://www.njp.org/)
Received 22 May 2002, in final form 25 July 2002
Published 6 September 2002

Abstract. The role of large-scale fluctuation structures in electrostatic drift-wave-type plasma turbulence is highlighted. In particular, well-defined laboratory experiments allow one to study the dynamics of drift wave mode structures as well as 'eddies' in drift wave turbulence. In the present paper we discuss the mutual relationships between observations made in linear magnetic geometry, purely toroidal geometry and magnetic confinement. The simplest structure, a saturated, nonlinear drift mode, is the starting point for a Ruelle–Takens–Newhouse transition route to chaos and weakly developed turbulence. Both spectral and phase space analysis are applied to characterize in detail the transition scenario, which is enforced due to an increased drive by the plasma equilibrium state. In addition to direct multi-probe observation, statistical approaches are most revealing for the systematic study of the spatiotemporal dynamics in fully developed drift wave turbulence. In particular, the propagation of large-scale 'eddy' structures is traced by conditional statistics methods. Finally, the control of drift wave turbulence by spatiotemporal synchronization is discussed.

1. Introduction

A key issue in turbulence research is the formation, motion and decay of large-scale fluctuation structures. Prominent examples in neutral fluids are Kármán vortices that eventually form in the flow past a solid obstacle [1, 2]. The build-up of large-scale (coherent) spatial structures is due to self-organization processes, which are closely related to large differences in the decay rates of the average invariants of the turbulence [3]. Those concepts essentially remain valid

1367-2630/02/000067+23$30.00

for magnetized plasmas, e.g. in magnetohydrodynamic (MHD) turbulence [4], which is often observed in strongly dynamic events like disruptive processes in tokamaks or solar flares.

Due to tremendous recent progress in theory and computer simulation of plasma turbulence, the knowledge of large-scale structures in turbulence has greatly increased. Since turbulence in general is of a spatiotemporal nature, the corresponding experimental work is a challenge, in particular in fusion devices where spatially resolved fluctuation measurements are often difficult to do.

In the present paper we focus on recent laboratory experiments on the dynamics of large-scale spatial structures in magnetized plasmas. With laboratory experiments a highly controllable experimental plasma device is used that is optimized for turbulence research with spatially and temporally resolved diagnostic tools available. Typically, such devices are smaller, low-temperature discharge devices and can be operated in steady state in order to achieve equilibrium conditions. The optimized set-ups and the accessible plasma provide the necessary wealth of information to make progress in the understanding of turbulence in magnetized plasmas.

In this context, drift and flute modes are two most important instability mechanisms, appropriately described in a collisional two-fluid picture [5]. They are low frequency $\omega \ll \omega_{ci}$, electrostatic, and are driven by the plasma density gradient perpendicular to the ambient magnetic field $\boldsymbol{B}$. The wavevector has its main component perpendicular to $\boldsymbol{B}$ with a scale length determined by the reduced gyro radius $\rho_s = \sqrt{m_i T_e}/eB$ via the relation $k_\perp \rho_s \sim 1$ [6]. The frequency range corresponding to the observed wavenumbers is given by the diamagnetic frequency $\omega_\star(k_\perp) = k_\perp \rho_s C_s / L_\perp$, where $C_s = \sqrt{T_e/m_i}$ is the ion sound velocity and $L_\perp = n/\nabla_\perp n$ is the gradient length of the plasma density profile. Drift waves have a non-zero axial wavenumber component $k_{||} > 0$ and the perpendicular dynamics is tightly coupled to the electron response parallel to $\boldsymbol{B}$. Flute modes with $k_{||} = 0$ have no parallel dynamics.

Probably the first observations of drift waves were made in a linear magnetized laboratory experiment [7]. Independently, but around the same time, drift dynamics were theoretically investigated for linear instabilities [8]. In the subsequent years, a large body of work was produced both in theory and experiment, see e.g. [9]–[11] and references therein. The linear dynamics of drift waves can now be seen as fairly well understood. In the broad field of non-linear dynamics, in particular in turbulence, there is still a large number of open questions to resolve. One of these questions is the role of large-scale dynamical structures that spontaneously arise out of broad-band turbulence.

In drift wave and flute mode turbulence, the formation of large-scale structures is always observed and seems to be generic. As briefly described in section 2, already very simple drift wave models always show the spontaneous vortex formation [12]. Many aspects of large-scale structures are currently under investigation, e.g. the transition from stability to turbulence, the space–time dynamics of turbulent large-scale structures and their interaction with all other scales. This paper makes an effort to highlight some recent experimental aspects of the problem.

We finally note that the detailed role of large-scale structures in turbulent transport processes is still under investigation, but experiments as well as computer simulations indicate that strong transport 'events' are associated with localized convective particle motion [13]. Attempts to explain these observations are often based on sometimes ambiguous concepts and notions, like 'streamers' and 'self-organized criticality'. It is beyond the scope of the present work to address this and the transport aspect of large-scale structures.

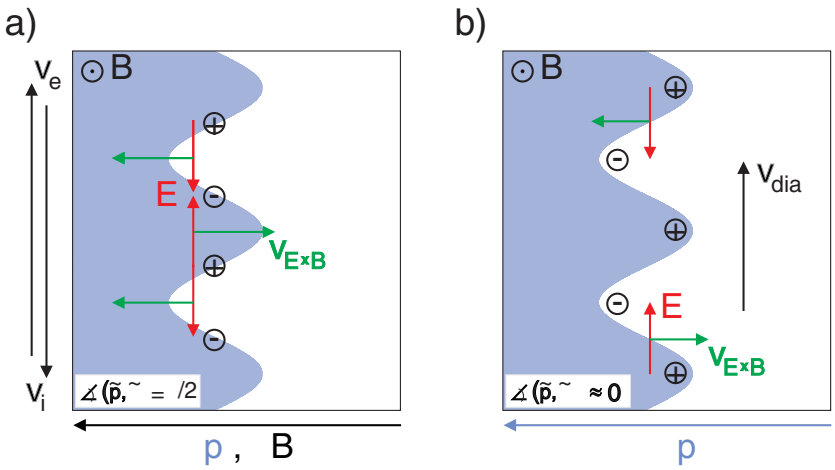

Figure 1. Instability mechanisms of curvature driven modes (a) and drift waves (b) in slab geometry.

The structure of the paper is as follows: after the introduction of the two instability mechanisms in section 2, the experimental set-ups and data analysis methods are briefly presented in section 3. The spatiotemporal behaviour of a single coherent drift mode, the transition scenario to turbulence and the statistical properties of large-scale fluctuation structures are discussed in section 4. The control of turbulence by externally applied electric fields is presented in section 5. The main findings are summarized and conclusions are drawn in section 6.

2. Basic instability mechanisms

Turbulence in the present experimental set-ups is governed by two different instability mechanisms, drift waves and curvature driven modes (flute modes). Both instabilities are driven by the background plasma pressure gradient, which is the source of free energy needed for the instabilities to develop. The basic mechanism of drift waves and curvature driven modes are schematically illustrated in figure 1. For ease of description a two-dimensional slab perpendicular to the magnetic field is shown. The initial state is a plasma pressure gradient ∇p with superimposed sinusoidal perturbation. Curvature driven modes (figure 1(a)) are the plasma analogy of the classical Rayleigh–Taylor instability in neutral fluids [14], whereby the curvature of the magnetic field replaces the gravitational force. The curvature and ∇B drifts, $\boldsymbol{v}_e$ and $\boldsymbol{v}_i$, lead to a separation of charge and consequently an electric field $\boldsymbol{E}$ perpendicular to the magnetic field $\boldsymbol{B}$ is generated. The resulting $\boldsymbol{E} \times \boldsymbol{B}$ drift amplifies the initial perturbation and becomes linearly unstable if the magnetic field gradient ∇B is in parallel to the plasma pressure gradient ∇p. This is the so-called unfavourable curvature region, as shown in figure 1(a). Stability is achieved if both gradients are anti-parallel, the favorable curvature region. The stability mechanism leads to a phase shift between the plasma pressure fluctuations and the plasma potential fluctuations of $\approx\pi/2$. Curvature driven modes are two-dimensional, i.e. the structures are elongated along the magnetic field with $\boldsymbol{k}_{\|} = 0$. The plasma dynamics parallel to the magnetic field becomes important if regions of unfavourable and favourable curvature regions are connected by the magnetic field,

e.g. due to rotational transformation of the magnetic field [15]. This leads to a variation of fluctuations along the magnetic field and consequently a non-zero parallel wavenumber $k_\parallel \neq 0$. In such a situation the fluctuation degree is larger in the unfavourable curvature region (ballooning) [16, 17].

In contrast to the curvature driven modes drift waves are intrinsically three-dimensional and the plasma dynamics parallel to the magnetic field is a crucial parameter for stability [18]. In figure 1(b) a homogeneous background magnetic field $\boldsymbol{B}$ is considered and the dynamics of electrons parallel to $\boldsymbol{B}$ is assumed to be adiabatic [19]. Consequently, a plasma pressure perturbation directly connects to a plasma potential perturbation via Bolzmann's relation and an electric field $\boldsymbol{E}$ perpendicular to $\boldsymbol{B}$ builds up. The $\boldsymbol{E} \times \boldsymbol{B}$ drift leads to propagation of the perturbation in the electron diamagnetic drift direction. In this relatively simple picture the initial perturbation is linearly stable due to the assumption of an adiabatic and instantaneous electron response parallel to the magnetic field. For linear instability the parallel dynamics must be inhibited, leading to a non-zero parallel wavenumber $k_\parallel/k_\perp \ll 1$ and a finite but small phase shift between plasma pressure and plasma potential perturbation [20]. Effects that lead to non-adiabaticity of electrons can be collisional processes [5], kinetic effects like Landau damping [21] or magnetic induction [22].

A deep insight into the dynamics of drift wave turbulence has been gained by numerical simulations. Basically, the simulations can be separated into two-dimensional models and a complete three-dimensional treatment. These two different approaches show significant differences in the context of the development of large-scale fluctuation structures and their role in the turbulent dynamics. In two-dimensional models the energy is generally cascaded inversely towards small wavenumbers (i.e. large-scale structures) as a result of the simultaneous conservation of energy and enstrophy [23]. Consequently, the energy of fluctuations develops towards the largest scales [24]. This is in contrast to the classical Rayleigh cascade, in which the energy is transported from the largest scales to the smallest [2, 25]. Common models depending on adiabatic parallel electron dynamics are based on the Hasegawa–Mima (HM) equation [26, 27]. Although the HM equation is somewhat oversimplified by the assumption of instantaneous parallel electron response the importance of large-scale fluctuation structures in drift wave turbulence was demonstrated and later verified in more advanced two-dimensional models, which also included non-adiabatic electrons [12, 28]–[31]. If fully three-dimensional numerical models are considered, large-scale fluctuation structures are less significant and a strict inverse energy cascade is generally not observed [32]. Usually, a minor part of the energy is transported to the large-scale structures but most of the energy is directly cascaded towards the small scales. Consequently, large-scale fluctuation structures are not as important as in two-dimensional models but they still form and are suggested to be of great important for transport processes perpendicular to the ambient magnetic field [33, 34]. If effects like magnetic shear or sheared flows are included in numerical models, which counteract the formation of large-scale fluctuation structures, the emergence of structures is further suppressed [35]. Figure 2 shows a comparison of numerical simulation results obtained from a two-dimensional HM-type model [28], figure 2(a), and a three-dimensional model including curvature and shear of the magnetic field, figure 2(b). In the two-dimensional case large fluctuation structures completely fill the simulation domain whereas in the three-dimensional case the structures are generally of smaller scale. In the latter large-scale structures still exist but their significance for the turbulent dynamics is weaker due to the different behaviour of the energy transport between spatial scales.

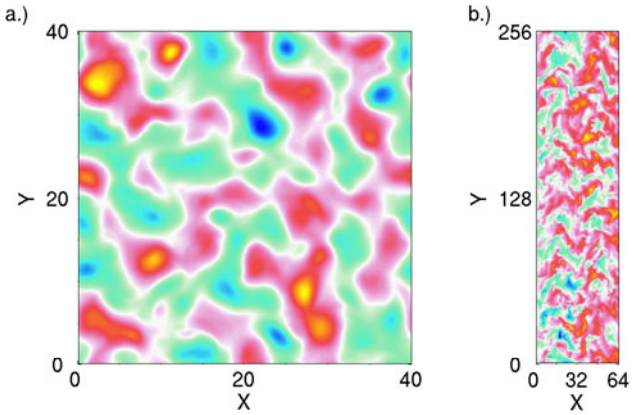

Figure 2. Results obtained from numerical simulations of a two-dimensional model (a) and a three-dimensional model (b). After [69].

3. Experimental set-ups and data analysis methods

To study the role of large-scale fluctuation structures, three different experimental set-ups are considered, mainly distinguished by their magnetic field geometry. The magnetic field configuration increases in complexity:

(i) homogeneous straight magnetic field,

(ii) purely toroidal magnetic field,

(iii) magnetic confinement, i.e. toroidal magnetic field with additional rotational transform.

3.1. Linear magnetic geometry

The linear, magnetized, low-β plasma device KIWI (figure 3) follows the original concept of the MIRABELLE device [36]. It consists of two plasma source chambers and a magnetized mid-section (magnetic field $B = 40$–100 mT). Argon plasma is produced in the source chambers by thermionic hot-cathode discharge in steady-state operation (typical neutral gas pressure $p = 3 \times 10^{-2}$ Pa, electron temperature $T_e = 1.2$–3.5 eV, electron density $n_e = 2 \times 10^{16}\ \mathrm{m}^{-3}$). Each source chamber is separated from the mid-section by a stainless-steel mesh grid (transparency $>60\%$). Only one chamber is operated as a plasma source. The grid at the active chamber is positively biased at U_g with respect to ground while the other grid, acting as loss surface, is kept at ground potential. In this way, electrons are injected into the mid-section and an $E \times B$ rotation of the plasma column as well as an axial electron current are established [37]. The magnetized plasma column is immersed in a stainless-steel tube, which is positively biased to predefine the potential at the azimuthal boundary (potential range $U_t = 0$–20 V). The spatiotemporal drift wave dynamics is observed using a circular array of 64 equally spaced cylindrical Langmuir probes [38], operated in the electron saturation current regime to measure density fluctuations. The time averaged plasma potential profile is parabolic and consequently the plasma $\boldsymbol{E} \times \boldsymbol{B}$ rotates as a rigid body. The time averaged plasma density profile is self-consistently connected to the linear radial electric field by classical transport and of Gaussian shape [39].

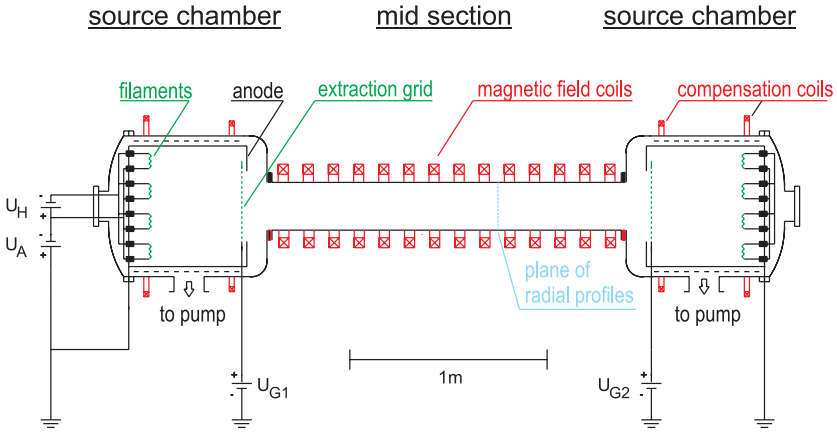

Figure 3. Schematic drawing of the linear triple-plasma device KIWI.

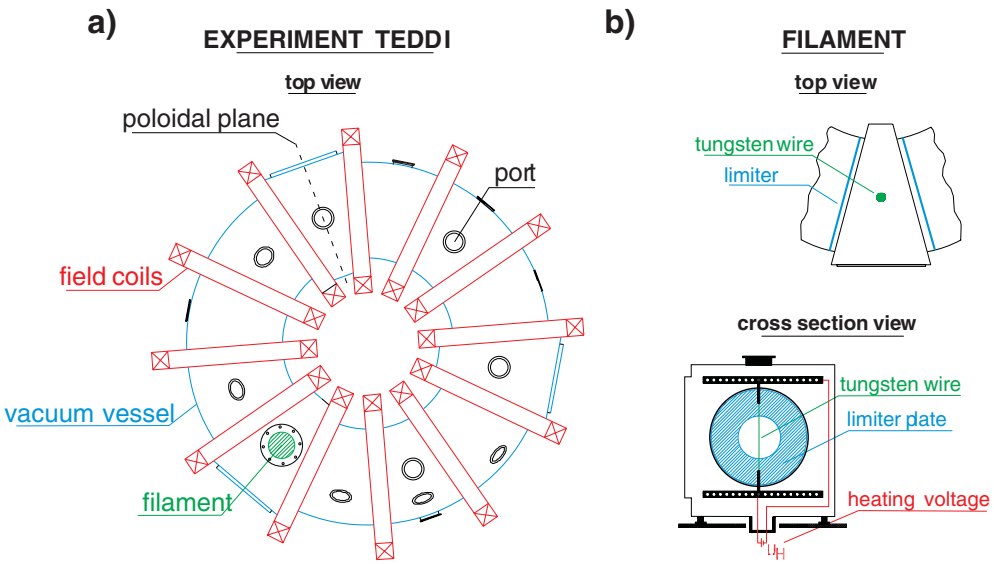

Figure 4. Schematic drawing of the TEDDI device (a) and the plasma source (b).

3.2. Simple toroidal geometry

To include magnetic curvature effects an experimental set-up with toroidal geometry is realized, the TEDDI device [40]. It belongs to the group of so-called simple magnetized tori (SMT), in which the magnetic field is purely toroidal [41]–[44]. A schematic drawing of the TEDDI device and the plasma source are shown in figures 4(a) and (b), respectively. It consists of three tube bends (large radius $R = 0.3$ m, small radius $r = 0.1$ m), connected by wedge-shaped segments where the plasma source is placed and measurements in poloidal cross sections are done. The vacuum vessel is immersed in planar poloidal magnetic field coils (maximum magnetic field on axis $B = 0.15$ T). The plasma is produced by a thermionic (filament) discharge. The tungsten filament is placed vertically inside the vacuum vessel and is directly heated by a current. The filament is negatively biased to ground. Poloidal limiters are placed on both sides of the source region and the plasma is produced by ionizing collisions between the primary

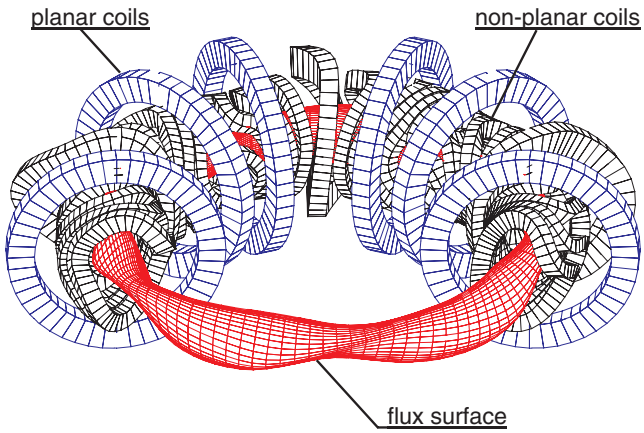

Figure 5. Magnetic coil system and shape of a magnetic flux surface of the W7-AS device.

electrons and the neutral argon gas background (neutral gas pressure $p = 3 \times 10^{-2}$ Pa, electron temperature $T_e = 4$ eV, plasma density $n = 1 \times 10^{16}$ m^{-3}). The main diagnostic tool for investigating the spatiotemporal dynamics of fluctuations are electric probes. It is well known that the plasma is MHD unstable in a purely toroidal magnetic field [45]. Owing to toroidal drifts the vertical charge separation produces an electric field, which accelerates the plasma radially outwards. Nevertheless, the discharge is steady state, but the poloidal plasma profiles are strongly asymmetric and are generally shifted outwards.

3.3. Toroidal magnetic confinement

The third experimental set-up used for studying large-scale fluctuation structures in electrostatic turbulence is the Wendelstein-7 AS stellarator [46, 47], schematically shown in figure 5. It is a $l = 2$, $m = 5$ stellarator [48], in which the magnetic field has a rotational transform to reach MHD stability [45]. The magnetic field is produced by 42 external non-planar magnetic field coils (maximum magnetic field on axis $B = 2.5$ T, rotational transform of $\iota = 0.25$–0.6). For the present experiments the plasma is produced by moderate electron cyclotron resonance (ECR) heating (edge electron temperature $T_e = 75$ eV, plasma density $n = 5 \times 10^{18}$ m^{-3}). Due to the pulsed operation, stationary plasma conditions are limited to a maximum temporal length of 800 ms. Measurements were done in the scrape-off layer (SOL), the very outside of the plasma, where the magnetic flux surfaces are intersected by limiters. Due to the high energy impact at the probes, a reciprocating probe array is used together with a fixed single probe, which provides the reference signal for the statistical analysis. The equilibrium plasma profiles inside the SOL are self-consistently determined by plasma transport perpendicular to the magnetic field across the last closed magnetic flux surface (LCMFS) field and plasma loss along the magnetic field to the limiters [49, 50].

3.4. Diagnostics and data analysis methods

Generally speaking, in turbulent systems one has to deal with temporally fluctuating, continuous field quantities, which are functions of both time and space. In experimental drift wave turbulence

research, the most common field quantities are plasma density $n(t)$, space charge potential $\phi(t)$, electron and ion temperature $T_{e,i}(t)$ and magnetic field $B(t)$. The first two are relatively easy to access by plasma probes, and for the moment we shall restrict ourselves to the two-field case.

The most basic assumption of many signal processing methods is ergodicity, which means that time average is equal to ensemble average [51]:

$$\langle\phi(t)\rangle = \int_{-\infty}^{\infty} \phi P(\phi)\,\mathrm{d}\phi = \lim_{T\to\infty} \frac{1}{T}\int_{-T/2}^{+T/2} \phi(t)\,\mathrm{d}t, \tag{1}$$

where $P(\phi)$ is the probability density of the fluctuating potential $\phi(t)$. It is convenient to assume zero-mean quantities $\langle\phi(t)\rangle = 0$, which can always be achieved by appropriate normalization. Based on equation (1), the usual linear signal processing tools can be systematically developed, namely auto- and cross-correlation functions $R(\tau) = \langle\phi(t)\phi(t+\tau)\rangle$ and $G_{n\phi}(\tau) = \langle n(t)\phi(t+\tau)\rangle$, respectively. The Wiener–Kintchine theorem relates them by Fourier transform to auto- and cross-power spectral densities [51].

Beyond such rather standard (linear) signal processing tools, more advanced techniques have been developed in turbulence research. Moments based on conditional probability densities may give a deeper insight into causalities [52], bispectra yield some information about mode coupling [53] and phase space analysis [54] is useful for studying the transition regime between regularity and turbulence. We refer to the cited references for an introduction to the different advanced signal processing methods, but we may comment subsequently on the key techniques used in the present work.

The conditional averaging (CA) method [52] was especially developed for the detection of large-scale fluctuation structures embedded into broad-band (mostly smaller scale) turbulence. Simultaneous recording of two signals is required, a space-fixed reference signal $\phi_r(t) = \phi(\boldsymbol{r}_0, t)$ and a space-resolved signal $\phi(\boldsymbol{r}, t)$. A preselected condition ϕ_c to be met by how the reference signal defines 'events', and CA yields some insight into the origin of events occurring at the reference position. A relatively short time series of length $[-\mathcal{T}/2, +\mathcal{T}/2]$ (with $\mathcal{T}$ as a free parameter) is recorded of both ϕ_r and ϕ at each time instant t_k and the condition ϕ_c is met. In this way, on the long term, an ensemble of $k = 1 \ldots N$ time series is collected and, by averaging, the incoherent part of the fluctuation is statistically suppressed. The formal procedure is

$$\phi_c(\boldsymbol{r}, \mathcal{T}) = \frac{1}{N}\sum_{k=1}^{N} [\phi(\boldsymbol{r}, t_k + \mathcal{T}) | \phi_r(t_k) = \phi_c]. \tag{2}$$

For a more detailed discussion, we refer the reader to [55].

Phase space analysis is nowadays a common tool for the analysis of chaotic data. Even though its meaning is limited in the case of fully developed turbulence, the phase space description can give additional insight into the dynamics of the nonlinear transition regime to developed turbulence, which is characterized by only a few degrees of freedom (e.g. modes). The 'true' phase space is spanned by the full set of time-dependent variables determining the dynamical state. In most experimental situations there is access to only one quantity $\phi(t)$. According to Taken's embedding theorem [56], a topologically equivalent phase space contour can be obtained by constructing the vector

$$\vec{\Phi}(t) = \begin{Bmatrix} \phi(t) \\ \phi(t+\tau) \\ \phi(t+2\tau) \\ \vdots \\ \phi(t+d\tau) \end{Bmatrix}, \tag{3}$$

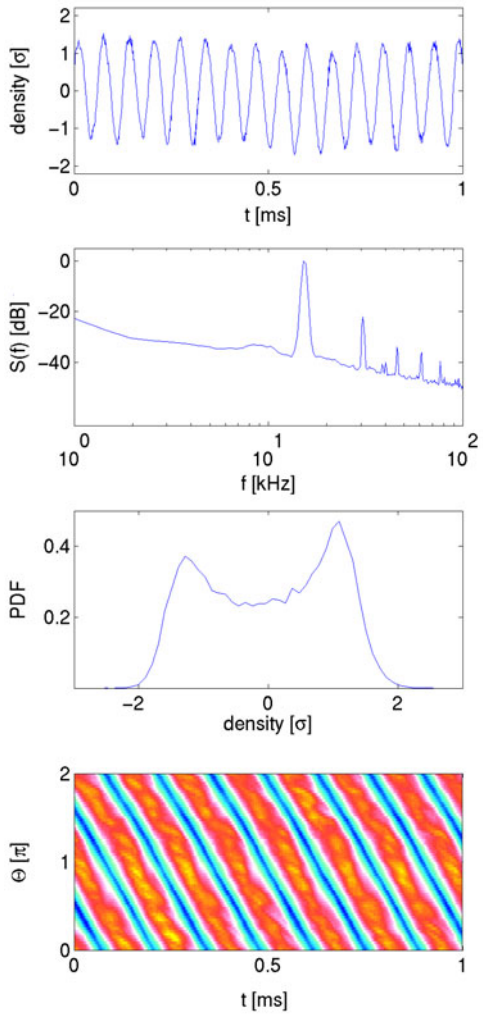

Figure 6. Time series of density fluctuations, corresponding power spectral density and PDF, and space–time diagram for a single $m = 2$ drift mode in the KIWI device.

where τ is an appropriately chosen delay time and d is the embedding dimension [54]. In principle, d has to be chosen to unfold the phase space structure appropriately, but visualization is often done in $d = 3$. If the number of degrees of freedom exceeds $d = 3$, the diagram must be seen as a projection of the actual phase space structure. The quantification of the geometrical and statistical properties of phase space structures is done by phase space analysis. Most common are ergodic measures, in particular the phase space dimension and the Lyapunov exponents [57]. The former characterizes the geometry of the phase space contour, the latter the stability of phase space orbits during time evolution.

4. Large-scale structures and transition to turbulence

4.1. Drift wave mode

Before discussing the properties of turbulent fluctuations in the different experimental set-ups, it is valuable to consider a coherent drift mode as observed in linear magnetic geometry (KIWI

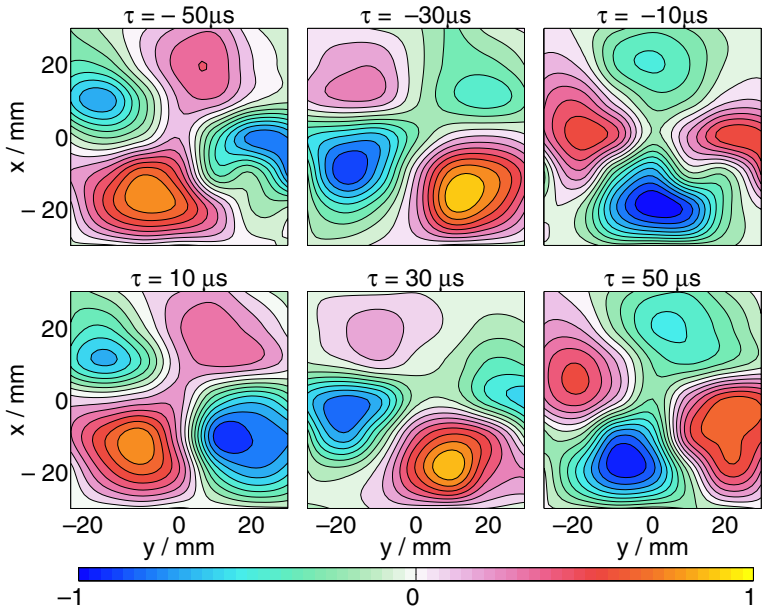

Figure 7. Results of CA for a $m = 2$ drift mode in a azimuthal cross section of the KIWI device. An animation is also provided.

device). Figure 6 compiles the time series of density fluctuations, the PDF and power density spectrum together with the space–time diagram. Density fluctuations are coherent as seen in the time series and the power spectrum $S(f)$, which is peaked at the Doppler-shifted drift frequency $\omega_\star = 15$ kHz and its higher harmonics. Consistent with the sinusoidal time series the PDF is double humped. The space–time diagram shows the typical picture of a $m = 2$ travelling wave with a phase velocity given by the slope of the stripes. The mode propagation is resolved in a two-dimensional cross section perpendicular to the magnetic field by means of CA. Figure 7 shows the result of the analysis for a time interval of $\tau = -50 \cdots + 50$ μs. An animation for better visualization is also provided. The ambient magnetic field points out of the plane. The $m = 2$ mode structure is clearly observed. The maximum amplitude is located in the maximum density gradient region and the structure propagates with the Doppler-shifted diamagnetic drift, which is counterclockwise in this representation. The spatial extent of the drift mode is of the order of the radial plasma size.

4.2. Route to drift wave turbulence

A well-defined transition scenario from laminar to turbulent flows, namely the Ruelle–Takens–Newhouse (RTN) scenario, has been predicted by dynamical systems theory [58] and was observed for the first time in driven neutral fluid flows [59]. Later, a two-fluid computer simulation revealed a similar behaviour in a magnetized plasma as well [60]. In a highly controllable plasma experiment the RTN transition from a completely stable state to weakly developed turbulence [61] was explicitly demonstrated. We subsequently recall this work to highlight the role of large-scale structures in the transition process.

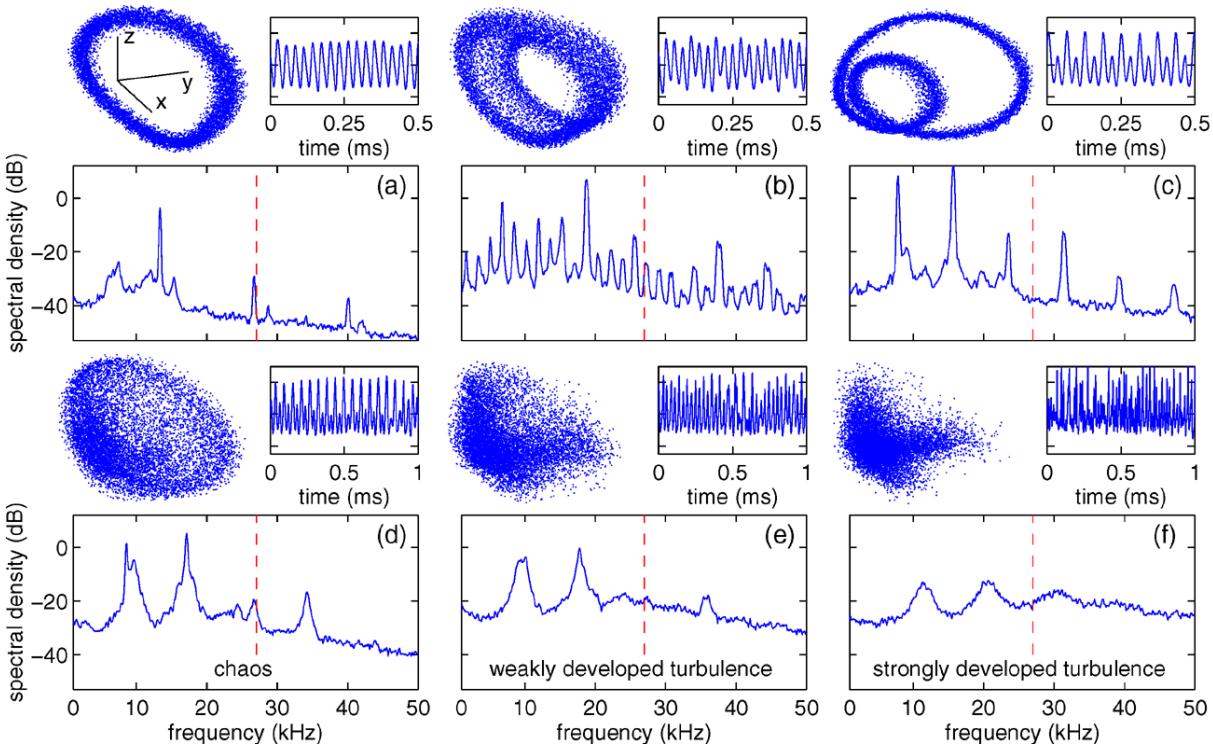

Figure 8. Transition to turbulence in the KIWI device. Shown are the phase space diagrams, time series, and power spectral densities of density fluctuations for different control parameters $\epsilon = 0 \ldots 1.01$. Animations of the phase space and sound files of the density fluctuations are provided.

Figure 8 compiles a series of diagrams showing the 3d phase space diagram, the time series of plasma density fluctuations and the corresponding power spectral densities for increasing control parameter $\epsilon = (U_g - U_{gc})/U_{gc}$. At $\epsilon = 0$ (resp. $U_g = U_{gc}$, the critical grid bias) a single drift wave mode sets on and saturates after a few cycles (frequency $f_3 = 13.5$ kHz). Figure 8(a) shows the single-mode state at $\epsilon = 0.14$. Nonlinear instability leads to parametric wave decay [62] and, as a result, just above $\epsilon = 0.33$, a second, lower frequency drift mode (frequency $f_1 = 6.9$ kHz) emerges (figure 8(b)). The nonlinear interaction between the two drift modes becomes evident by the large number of side-bands at $nf_3 \pm mf_1$ $(n, m = 1, 2, 3, \ldots)$. The corresponding time series shows a quasiperiodic amplitude modulation and the phase space contour is a torus, as expected. Slightly above $\epsilon = 0.5$, the idler mode at $\approx$15 kHz rapidly grows in amplitude and mode-locks to the drift mode at $\approx$7.5 kHz. In such a mode-locked state (figure 8(c)), the two low-frequency modes dominate the dynamics and, due to their resonant interaction, no side-bands occur except for higher harmonics. The phase space contour is a two-orbit and the time series shows a two-periodicity. At higher control parameter values, above $\epsilon \approx 0.7$, the mode-locked state is gradually destabilized and the peaks in the power spectrum become significantly broader (figure 8(d)). The phase space two-orbit is filled up and the time series shows how the two-periodicity is subjected to an additional, low-frequency modulation. The transition from weakly developed to developed turbulence is smooth and accompanied

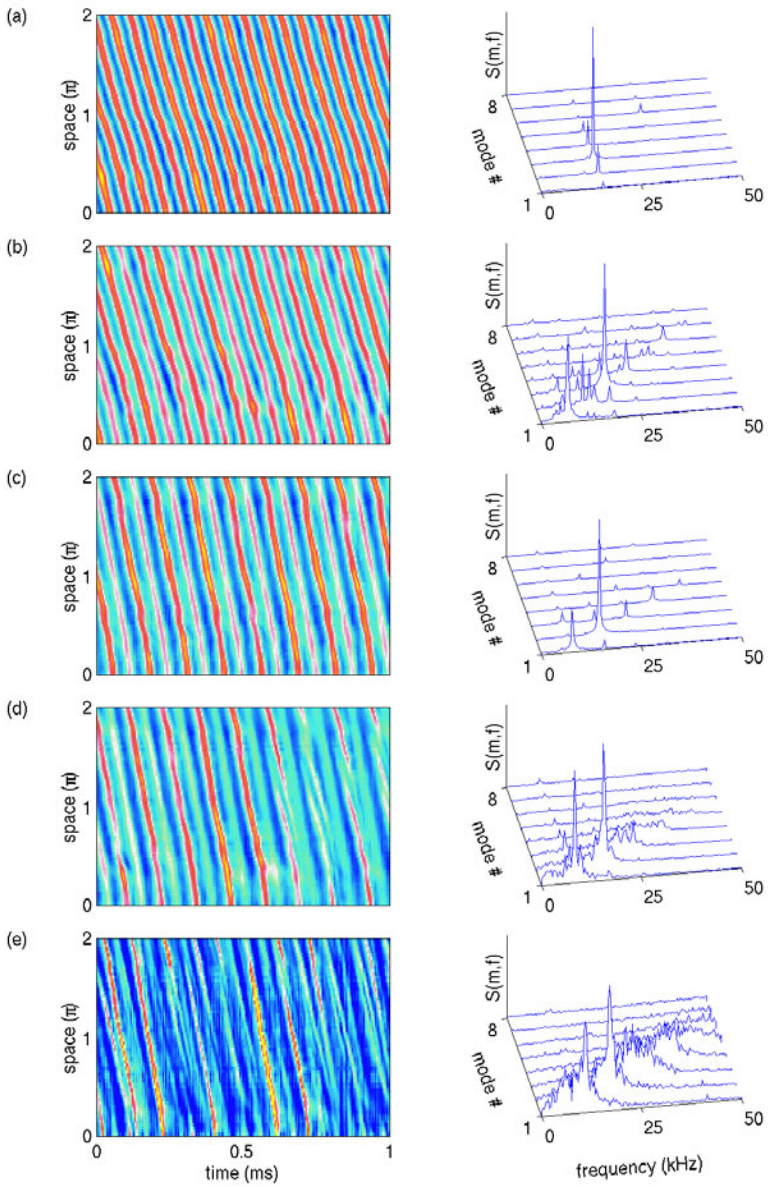

Figure 9. Space–time diagrams and wavenumber–frequency spectra for the different dynamical states of density fluctuations in the KIWI device for different control parameters $\epsilon = 0 \ldots 1.01$.

by increasingly broad power spectra, unstructured phase space and irregular time evolution of density fluctuations (figures 8(e) and (f)). For illustration, the phase space diagrams are also shown as an animation where the time evolution of the trajectories becomes evident. Also provided are sound files of the different drift wave dynamics, which is mostly found in the audible frequency regime.

Of particular interest are the space–time dynamics of drift waves. As mentioned above, probe arrays may provide a sufficient spatial resolution to observe at least the large-scale

structures with $k < 0.3\ \mathrm{m}^{-1}$. Figure 9 shows space–time diagrams and the corresponding frequency–wavenumber spectra of the above described transition to turbulence. As a general trend, for increasing control parameter ϵ, the space–time diagram becomes more complex and the power spectrum broadens. At $\epsilon = 0.13$ (figure 9(a)), a regular $m = 3$ drift mode is established. Correspondingly, there is only one peak in the power spectrum for $m = 3$ at 12.5 kHz. The quasiperiodic case, $\epsilon = 0.49$, is shown in figure 9(b). Careful inspection of the space–time diagram reveals a quasiperiodic amplitude modulation both in time and in space. Consequently, the peaks in the power spectrum distribute in the (f, m) plane. Note, for instance, that the $m = 2$ idler mode corresponds to several peaks at different frequencies. The bifurcation to the mode-locked state, $\epsilon = 0.62$, is shown in figure 9(c). The strict two-periodicity in space and time is also seen in the power spectrum, where the $m = 1$ mode appears as the (lower amplitude) sub-harmonic of the $m = 2$ mode, the former idler. The mode-locked state is gradually destabilized for increasing control parameter. In figure 9(d), the space–time diagram reveals the occasional occurrence of phase defects (at $t = 0.6$–0.9 ms), which directly lead to spectral broadening. These phase defects become more and more frequent until at $\epsilon = 1.01$ the drift wave turbulence is fairly well developed with a broad power spectrum and a rather irregular space–time mode pattern. This transition to turbulence is known as the RTN scenario [63].

4.3. Turbulent structures

In section 4, the transition scenario to turbulence in the KIWI device was outlined. We subsequently discuss the statistical properties of the developed turbulent state ($\epsilon = 1.01$), which establishes after the RTN scenario. In figure 10 a time series of turbulent density fluctuations, the corresponding PDF and power spectral density and a space–time diagram are shown. In contrast to the single coherent drift mode (figure 6) the time series shows an irregular behaviour with preference to large positive fluctuation events. This behaviour is quantified by a Gaussian-like PDF with a significant skewness of $s = 0.59$. In the corresponding power spectral density the remaining dominant peaks are broadened and a power law scaling $f \propto f^{-\alpha}$ at frequencies above 50 kHz is observed ($\alpha \approx 3$). Irregularity of density fluctuations is found in both the temporal behaviour and the spatiotemporal development. Several pronounced structures are observed in the space–time diagram, propagating in the electron diamagnetic drift direction (also parallel to the $\boldsymbol{E} \times \boldsymbol{B}$ rotation of the plasma). The dynamics of such structures is more complicated and does not show the coherent behaviour as in the single-mode case. They appear occasionally, have a finite lifetime and show frequent phase dislocations. To elucidate the dynamics of the turbulent structures, CA of density fluctuations has been done covering the azimuthal plane. The results are shown in figure 11 for a time interval of $\tau = -36 \cdots + 36\ \mu$s. The formation of a positive fluctuation structure is found at $\tau = -36\ \mu$s. The spatial scale of the structure is comparable to the size of the coherent drift modes with a radial extent of $\approx 2\rho_s$. Although the time averaged plasma profiles are unaffected by the turbulent fluctuations, the structure's propagation during the first half of the time window deviates from pure azimuthal movement. Instead, it propagates radially outwards. In the second half of the time window the propagation is azimuthal in electron diamagnetic drift direction until its final decay. At $\tau = 0$ the structure is detected at the reference position, showing that a single structure is responsible for the detected events in the reference signal. During the early phase of structure formation, a negative density fluctuation structure develops as well, but with a strongly reduced lifetime. The dynamics seen in figure 11 is consistent with the space–time diagram, figure 10. In particular the partially

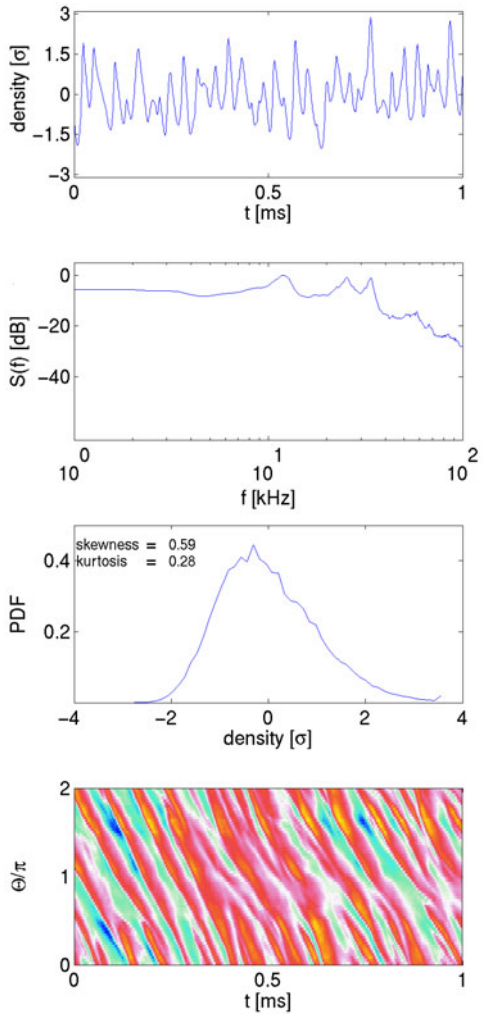

Figure 10. Time series of turbulent density fluctuations in the KIWI device, corresponding power spectral density and PDF, and space–time diagram.

azimuthal propagation leads to stripe-like patterns, which disappear if the structure propagates radially inwards out of the observation circumference of the probe array. Alternatively, the structure just decays. Comparison between plasma density and plasma potential fluctuations yields a small phase shift of $\angle(\Phi, n) \approx 0$, consistent with the conventional drift wave picture (cf figure 1).

Due to strong gradients and curvature of the magnetic field no single modes are observed in the TEDDI and the plasma in this set-up is always in a fully developed turbulent state. Figure 12 shows a time series of density fluctuation, the corresponding power spectral density and the PDF. The time evolution of fluctuations is irregular and the PDF is slightly skewed towards positive density fluctuations (skewness $s = 0.42$). Different from fluctuations in the KIWI plasma the power spectral density shows no dominant peaks and a power law scaling over a wide frequency range of one decade. This indicates fully developed turbulence. The dynamics of large-scale structures obtained by CA is shown in figure 13 for a time interval $\tau = -80 \cdots + 80\ \mu$s. Large-

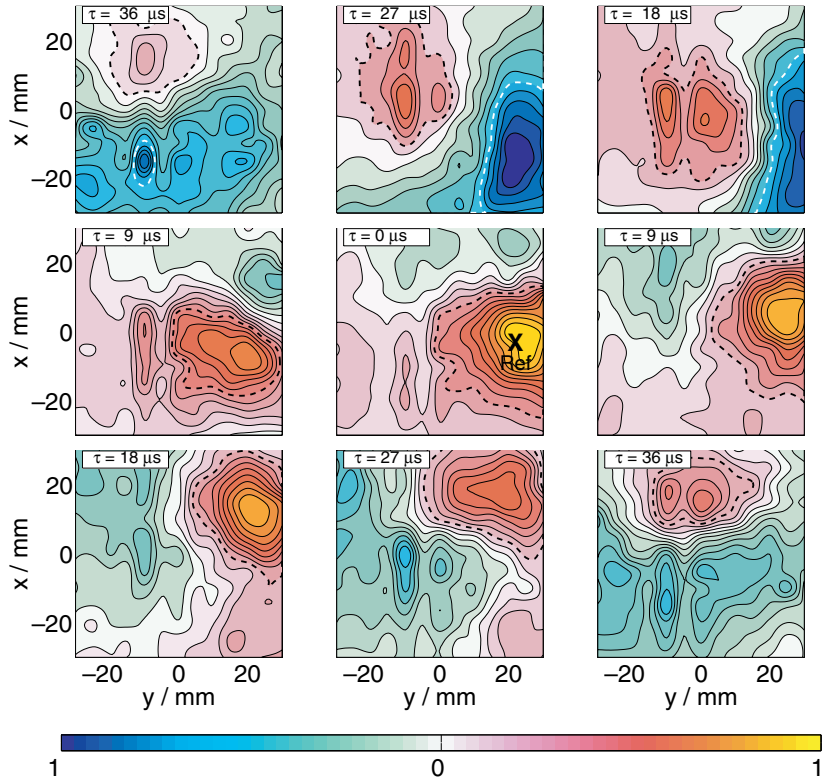

Figure 11. Results of CA of turbulent density fluctuations in the KIWI device for an azimuthal cross section. The maximum and minimum structures are highlighted by black and white contour lines, respectively. An animation is also provided.

scale structures are found in the full time range. The extent of structures is of the order of the plasma size ($\approx 6\rho_s$). At $\tau = -80\,\mu$s a minimum structure in the plasma centre and two maximum structures shifted to the outer limiter edge develop. During the first half of the time window the minimum structure propagates radially outwards, but during the second half the propagation is mainly poloidal. During its lifetime the structure is distorted. The spatiotemporal development of the maximum structure is similar to the minimum structure. On the outside the propagation is mainly in the poloidal direction, whereas in the plasma centre the propagation is primarily radial. In the animation provided with figure 13 the temporal evolution of the large-scale structures is compared to the time averaged plasma potential profile, shown as contour lines. It turns out that the propagation of structures is fully determined by $\boldsymbol{E}\times\boldsymbol{B}$ convection, whereby the time averaged equipotential contour lines act as streamlines for the large-scale turbulent structures [64]. Due to the nonexistence of MHD equilibrium in the pure toroidal magnetic field configuration of the TEDDI device the poloidal time averaged plasma potential profile is asymmetric and convection is radial in the plasma centre and poloidal in the outer limiter region. The distortion of structures is most likely due to velocity shear [35]. The phase shift between plasma density and potential fluctuations is found to be $\angle(\Phi, n) \approx \pi/2$ and no variation of fluctuations along the magnetic field is observed. This suggests curvature driven modes as the basic instability mechanism (cf figure 1).

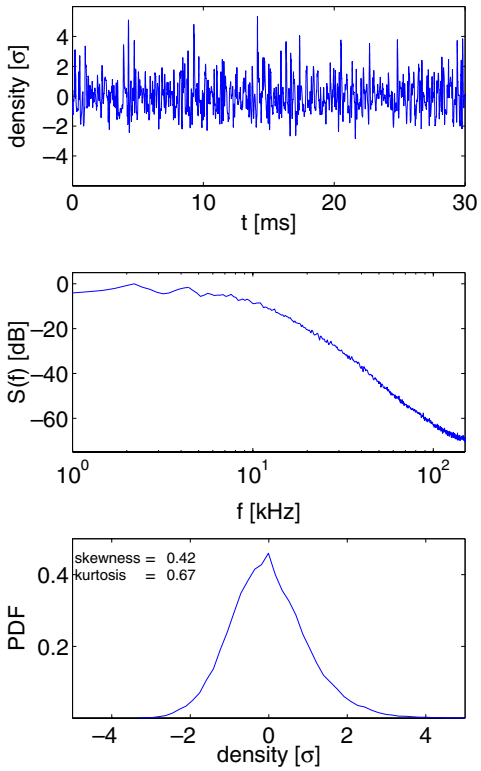

Figure 12. Time series of turbulent density fluctuations in the TEDDI device, corresponding power spectral density and PDF.

Similar to the TEDDI device fully developed turbulence is always observed in the SOL of W7-AS. An overview about basic properties of potential fluctuations, i.e. the time series, the power spectral density and the PDF, is given in figure 14. The temporal evolution of fluctuations is irregular and the PDF is of almost perfect Gaussian shape. In the corresponding power spectral density no dominant peaks are observed and the decrease is given by a power law scaling over one frequency decade. CA has been applied to the fluctuations to observe the spatiotemporal development of large-scale structures. The result over a time interval of $\tau = -8 \cdots + 20\ \mu$s is shown in figure 15. The observation area is inside the SOL limited by the probe array size in poloidal direction. The LCMFS is located at $r = 0$ mm. A large-scale structure is clearly observed. It enters the observation area at $\tau = -4\ \mu$s and propagates in pure poloidal direction before it starts to decay at $\tau = 8\ \mu$s. Thus, the propagation is strongly aligned to the magnetic flux surface. The radial extent of the structure is $\approx$15 mm corresponding to $\approx 10\rho_s$ and the structure is elongated poloidally. This is most likely due to the sheared $\boldsymbol{E} \times \boldsymbol{B}$ velocity in the SOL. In contrast to the KIWI and TEDDI configuration the lifetime of the observed structure is considerably smaller. Comparison of its lifetime to its rotation period, the eddy turnover time, yields that the structure is not coherent in the strict sense [35]. CA of density fluctuations provides similar results about the lifetime and extent of observed structures. It was shown that density fluctuation structures are somewhat causally determined by potential fluctuation structures due to $\boldsymbol{E} \times \boldsymbol{B}$ convection of the potential structure in a radial density gradient [65]. The phase shift between plasma density and potential fluctuations is found to be $\angle(\Phi, n) \approx \pi/2$, which hints at curvature driven modes as the basic instability mechanism (cf figure 1).

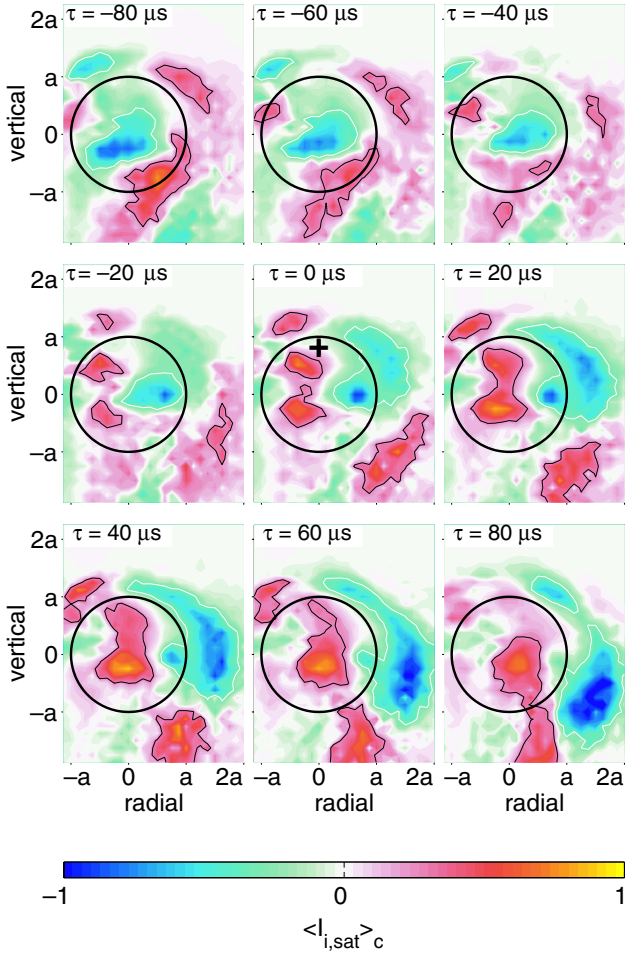

Figure 13. Results of CA of turbulent density fluctuations in the TEDDI device for a poloidal cross section. The poloidal limiter is indicated as a solid black circle. Maximum and minimum structures are highlighted by black and white contour lines, respectively. The cross at $\tau = 0$ μs indicates the position where the reference signal for CA is measured. An animation is also provided.

5. Control of turbulent dynamics

Drift wave chaos was successfully controlled in a recent experiment by using continuous delay-time feedback techniques [66]. However, as discussed above, low-dimensional chaos exists only in a narrow control parameter regime during the transition route to turbulence [61]. A different, more robust method is open-loop control (also called synchronization) acting in both space and time [67]. The experiment is done as follows [68]: a special arrangement of eight stainless-steel electrodes (octupole exciter) is positioned in flush-mounted geometry in the edge region of the plasma column. The electrodes of the octupole exciter are driven by sinusoidal signals with a fixed, preselected phase angle θ between each electrode pair. This generates an azimuthally rotating electric field which turns out to select a single mode out of the broad drift wave turbulence spectrum [68].

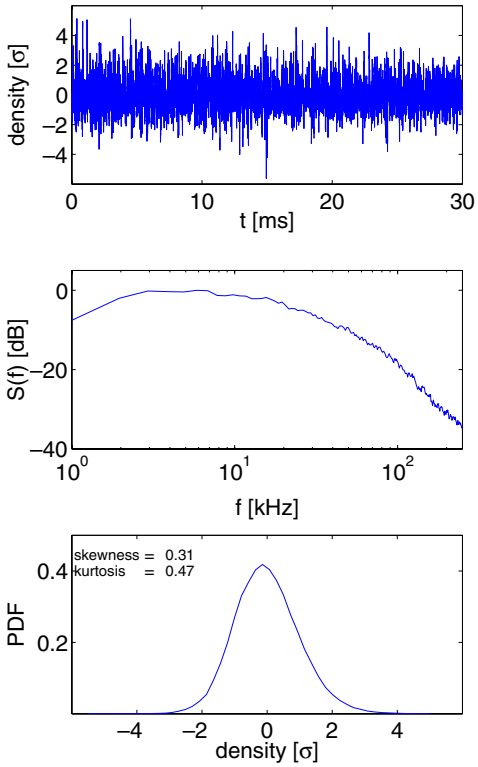

Figure 14. Time series of turbulent potential fluctuations in the SOL of the W7-AS, corresponding power spectral density and PDF.

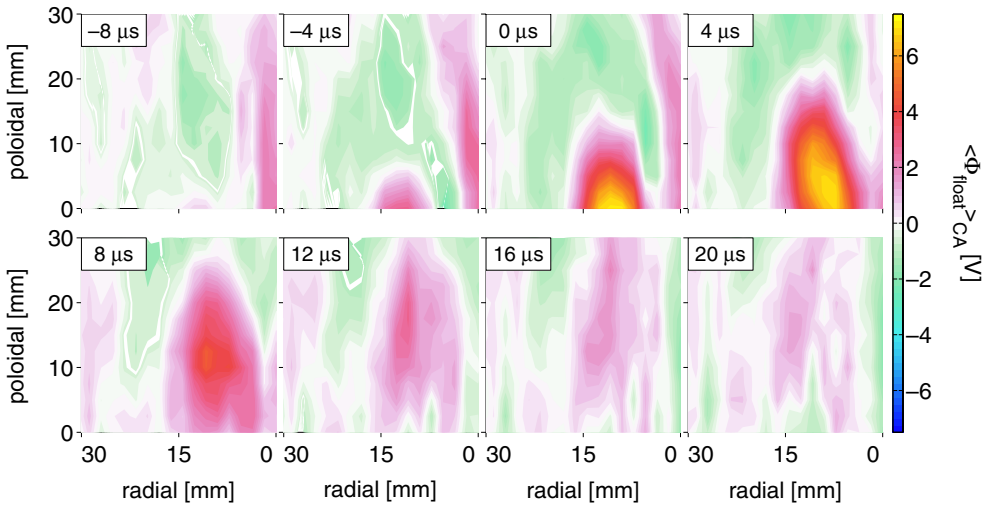

Figure 15. Results of CA of turbulent potential fluctuations in the SOL of W7-AS in a poloidal cross section.

In the linear magnetized plasma device MIRABELLE, drift wave turbulence is created by choosing values $U_g = 5$ V and $U_t = 12$ V. The result is depicted in figure 16(a). The space–time diagram of density fluctuations is dominated by irregular features and no defined mode structure is observed [61, 37]. For mode-selective synchronization of drift wave turbulence, a

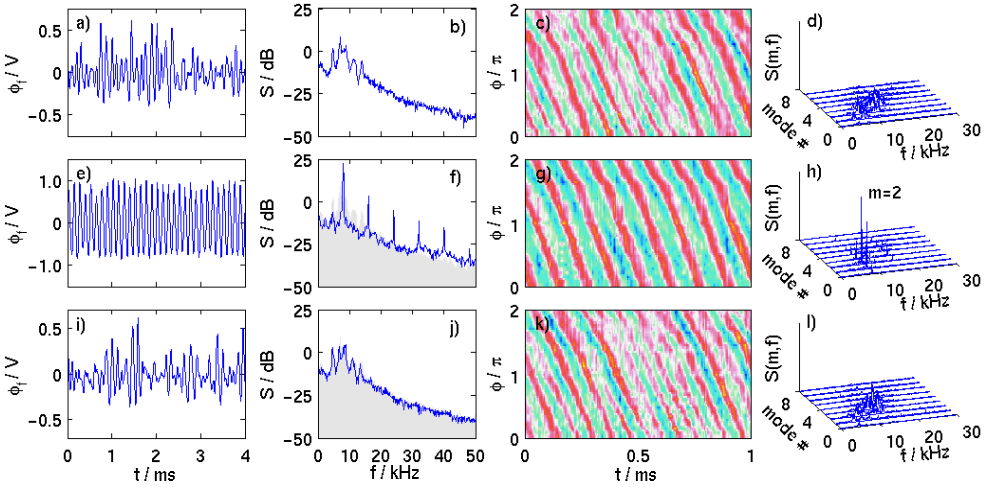

Figure 16. Time series, power spectral densities, space–time diagrams and wavenumber–frequency spectra of experimentally obtained density fluctuations in the MIRABELLE device without external control (top row), with co-rotating control signal (middle row) and with counter-rotating control signal (bottom row). The shaded areas in (f) and (j) indicate for comparison the power spectral density without control signal (b).

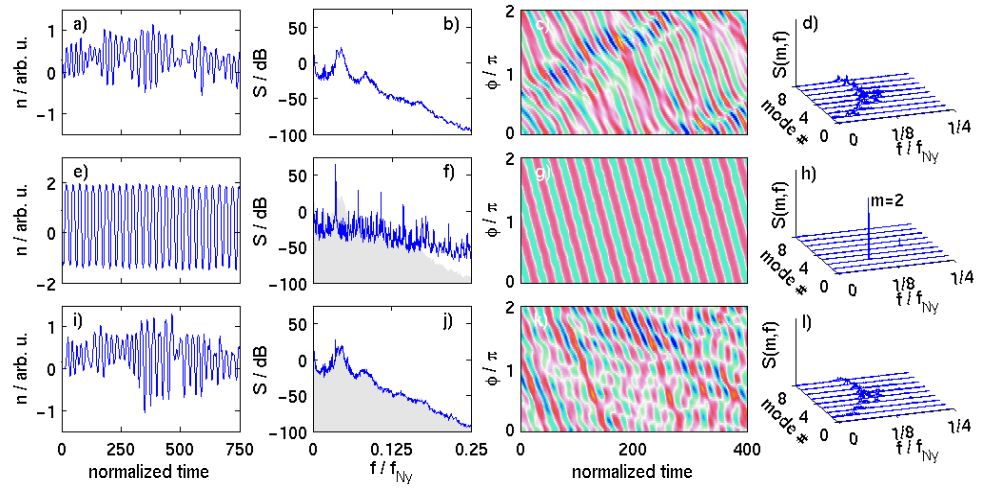

Figure 17. Time series, power spectral densities, space–time diagrams and wavenumber-frequency spectra of the numerical simulation based on the Hasegawa–Wakatani equations in the same representation as figure 16.

driver frequency f_d is applied to the octupole exciter. f_d is chosen to be close to pronounced spectral features in the low-frequency regime of the power spectrum. The azimuthal mode number m_d is predetermined by selecting a phase shift $\theta = m_d\pi/4$. The so-obtained exciter signal drives a specific drift mode with phase velocity $v_\phi = f_d 2\pi r_x/m_d$, which must be compatible with the drift wave dispersion. r_x is the radial position of the exciter electrodes. Choosing $m_d = 2$, driver frequency $f_d = 8.0$ kHz and driver amplitude $A = 1.0\,\mathrm{V}$ the large-scale drift wave turbulence is successfully synchronized as shown in figure 16(b). Note that

smaller scale structures, corresponding to mode frequencies above 20 kHz, remain essentially unchanged by the synchronization signal. In the space–time diagram, large-scale regular dynamics dominate, i.e. a pronounced mode structure with the preselected $m = 2$ is observed. To test if the control effect is really a spatiotemporal one, we simply reverse the sign of θ and thus the rotation direction of the exciter field. In contrast to the co-rotating case, the counter-rotating exciter signal is moving at $\sim 2v_\phi$ in the drift wave frame and a much weaker synchronization effect is expected. Figure 16(c) clearly confirms that a counter-rotating exciter field has almost no influence on the drift wave turbulence and on the time averaged plasma profiles at all.

The experimental results have been theoretically confirmed by a standard drift wave model, the Hasegawa–Wakatani equations [28], for density and vorticity fluctuations. The exciter itself is modelled by assuming that it gives rise to an additional oscillating parallel current profile of the functional form

$$\nabla_\parallel J_{ext} = \tilde{A} \sin(\pi r/r_0) \sin(2\pi m_d \Theta - \omega_d t) = \hat{S}, \tag{4}$$

where r_0 is the radius of the plasma and Θ is the poloidal coordinate. Further details are found in [27]. The simulation result is shown in figure 17. By comparing figures 16 and 17 it becomes evident that the experimental findings discussed above are fully reproduced by the simulation. Starting with unperturbed drift wave turbulence (a), a synchronized $m = 2$ state is achieved at relatively small driver amplitude, $\tilde{A} = 0.75$, if a co-rotating current profile is applied (b). Exactly as in the experiment, a counter-rotating current profile of the same amplitude has almost no effect (b). We may conclude that the experiment is at least qualitatively reproduced by the 2d model. The rotating current profile couples via $\nabla_\parallel J_{ext}$, the two equations mode-selectively and thus leads to amplification of the preselected mode m_d. In other words, in the drift wave frame the poloidal symmetry is broken by the structured current profile which leads to mode selection. For a more profound analysis we refer the reader to [68].

6. Summary and conclusions

To summarize, two different instability mechanisms in magnetized plasmas—drift waves and curvature driven modes—have been experimentally studied in three different experimental configurations: linear, purely toroidal and helical magnetic field geometry. The discussion focuses on the role of large-scale structures in the transition to turbulence, the characterization of specific properties of these structures in the different experimental set-ups, and how control of the turbulent dynamics by influencing the largest scales can be achieved.

A common feature of all three configurations is the presence of large-scale structures embedded in broad-band turbulence, which is also observed in plasma turbulence models.

In linear magnetic field geometry the dynamical state is controlled by the axial boundaries, which determine the plasma current and plasma rotation. Via the external current circuit the transition from stability to weakly developed turbulence can be studied in its very detail. It turns out that the RTN scenario, known from neutral fluids, is followed. During the transition the periodicity of the single drift mode is lost and a weakly developed turbulent state is achieved, which is characterized by the sporadic occurrence of large-scale coherent structures. The analysis of these structures by CA suggests that these are reminiscences of the single drift mode. The structures have a finite but relatively long lifetime and propagate mainly in the azimuthal direction at $\boldsymbol{E} \times \boldsymbol{B}$ velocity, but also have a radial velocity component. The spatial scales of the structures

are of the order of the plasma size and turbulent convection processes by these structures affect the entire plasma volume.

In purely toroidal magnetic geometry the plasma is always in a fully developed turbulent state. The observed structures are identified as being caused by curvature driven instability. The structures have a remarkably long lifetime and can have a size up to the plasma dimensions. In this sense they are comparable to the structures found in linear magnetic field geometry. Here, the partly radial propagation of the observed large-scale structures is along the time averaged equipotential lines, which are asymmetric and determined by the turbulence itself and not by a MHD equilibrium.

Finally, in helical (stellarator) magnetic field geometry fully developed turbulence in the SOL is driven by strong gradients and magnetic curvature. The properties of the observed large-scale structures differ from the above situations. The lifetime is shorter than the eddy turnover time. Thus, the structures are not coherent in the strict sense. The radial extent of structures is much smaller than the plasma size, so that no global convection process caused by these structures exists. Due to MHD equilibrium the propagation is purely in poloidal direction on the magnetic surface and is determined by $\boldsymbol{E} \times \boldsymbol{B}$ rotation of the plasma.

The synchronization of the weakly developed turbulence of the linear device clearly demonstrates that suppression of turbulence occurs in the small frequency regime of fluctuations, which can be addressed to the large-scale structures. By external application of rotating electric fields only the preselected single drift mode propagates and the small-scale fluctuation spectrum remains essentially unchanged. This clearly demonstrates the dominance of the large-scale structures in the turbulent dynamics.

In conclusion, the occurrence of large-scale structures seems to be a generic feature of turbulence based on drift waves and curvature driven modes, independent of the specific magnetic field configuration and the boundary conditions. The observed specific properties of structures such as lifetimes and spatial extents cannot be attributed to the basic underlying instability mechanisms. The observations, in fact, suggest that large-scale structures may either be a reminiscence of a destabilized mode structure or the result of inverse cascading from small scales. Consequently, plasma as well as boundary conditions have a strong influence on the formation of large-scale structures by directly affecting the driving parameters of the instability itself or by affecting the governing cascading direction.

References

[1] Van Dyke M 1982 *An Album of Fluid Motion* (Stanford, CA: The Parabolic Press)
[2] Frisch U 1995 *Turbulence: The Legacy of A N Kolmogorov* (Cambridge: Cambridge University Press)
[3] Biskamp D and Schwarz E 2001 *Phys. Plasmas* **8** 3282
[4] Biskamp D 1993 *Nonlinear Magnetohydrodynamics* (New York: Cambridge University Press)
[5] Horton W 1999 *Rev. Mod. Phys.* **71** 735
[6] Catto P J, El Nadi A M, Liu C S and Rosenbluth M N 1974 *Nucl. Fusion* **14** 405
[7] D'Angelo N 1963 *Phys. Fluids* **6** 592
[8] Moiseev S S and Sagdeev R Z 1963 *J. Exp. Tech. Phys.* **17** 515
[9] Chen F F 1965 *Phys. Fluids* **8** 1323
[10] Hendel H W, Chu T K and Politzer P A 1968 *Phys. Fluids* **11** 2426
[11] Yamada M and Hendel H W 1978 *Phys. Fluids* **21** 1555
[12] Crotinger J A and Dupree T H 1992 *Phys. Fluids* B **4** 2854

[13] Terry P W 2000 *Phys. Plasmas* **7** 1653
[14] Komori A, Sato N and Hatta Y 1978 *Phys. Rev. Lett.* **40** 768
[15] Zeiler A and Biskamp D 1996 *Phys. Plasmas* **3** 2951
[16] Guzdar P N, Drake J F, McCarthy D, Hassam A B and Liu C S 1993 *Phys. Fluids* B **5** 3712
[17] Novakovskii S V, Guzdar P N, Drake J F and Liu C S 1995 *Phys. Plasmas* **2** 3764
[18] Chen F F 1965 *Phys. Fluids* **8** 1323
[19] Horton W and Hasegawa A 1994 *Chaos* **4** 227
[20] Scott B 2000 *Phys. Plasmas* **7** 1845
[21] Jenko F and Scott B D 1999 *Phys. Plasmas* **6** 2418
[22] Scott B 1997 *Plasma Phys. Controlled Fusion* **39** 1635
[23] Kraichnan R H and Montgomery D 1980 *Rep. Prog. Phys.* **43** 547
[24] Fyle D and Montgomery D 1979 *Phys. Fluids* **22** 246
[25] Kolmogorov A N 1941 *Dokl. Akad. Nauk* **32** 16
[26] Hasegawa A and Mima K 1978 *Phys. Fluids* **21** 87
[27] Naulin V, Spatschek K H, Musher S and Piterbarg L I 1995 *Phys. Plasmas* **2** 2640
[28] Hasegawa A and Wakatani M 1983 *Phys. Rev. Lett.* **50** 682
[29] Terry P W and Horton W 1983 *Phys. Fluids* **26** 106
[30] Scott B D, Biglari H, Terry P W and Diamond P H 1991 *Phys. Fluids* B **3** 51
[31] Dupree T H 1967 *Phys. Fluids* **10** 1049
[32] Yoshizawa A, Itoh S, Itoh K and Yokoi N 2001 *Plasma Phys. Controlled Fusion* **43** R1
[33] Scott B D 1990 *Phys. Rev. Lett.* **65** 3289
[34] Scott B 1997 *Plasma Phys. Controlled Fusion* **39** 471
[35] Terry P W 2000 *Rev. Mod. Phys.* **72** 109
[36] Pierre T, Leclert G and Braun F 1987 *Rev. Sci. Instrum.* **58** 6
[37] Klinger T, Latten A, Piel A, Pierre T and Bonhomme G 1997 *Plasma Phys. Controlled Fusion* **39** B145
[38] Latten A, Klinger T, Piel A and Pierre T 1994 *Rev. Sci. Instrum.* **66** 3254
[39] Block D, Piel A, Schröder C, and Klinger T 2001 *Phys. Rev.* E **63**
[40] Greiner F, Grulke O, Lechte C and Piel A 2000 *Proc. 2000 Int. Congress on Plasma Phys. (Quebec City, Canada)* vol 1 pp 140–43
[41] Rypdal K, Grønvoll E, Øynes F, Fredriksen A, Armstrong R J, Trulsen J and Pécseli H L 1994 *Plasma Phys. Controlled Fusion* **36** 1099
[42] Singh R, Mahajan S and Avinash K 1996 *Phys. Rev. Lett.* **77** 1504
[43] Imbeaux F 1995 Etude des caracteristiques d´une colonne de plasma torique magnetise (Palaiseau, France: Laboratoire des Physique des Milieux Ionises, Ecole Polytechnique)
[44] Alba S, Fontanesi M, Galassi A, Riccardi C and Sindoni E 1993 *Phys. Essays* **6** 225
[45] Pfirsch D and Schlüter A 1962 *Max-Planck-Institut Report* MPI/PA/7/62
[46] Mathis R and Sapper J 1990 *Fusion Eng. Design* **11** 399
[47] Sapper J and Renner H 1990 *Fusion Tech.* **17** 62
[48] Boozer A H 1998 *Phys. Plasmas* **5** 1647
[49] Stangeby P C 2000 *The Plasma Boundary of Magnetic Fusion Devices (Series in Plasma Physics)* (Bristol: Institute of Physics)
[50] Stangeby P C 2000 *Plasma Phys. Controlled Fusion* **42** B271
[51] Priestley M B 1989 *Spectral Analysis and Time Series* 6th edn (San Diego, CA: Academic)
[52] Johnsen H, Pécseli H L and Trulsen J 1987 *Phys. Fluids* **30** 2239
[53] Kim Y C, Beall J M, Powers E J and Miksad R W 1980 *Phys. Fluids* **23** 258
[54] Abarbanel H D I 1996 *Analysis of Observed Chaotic Data* (New York: Springer)
[55] Huld T, Nielsen A H, Pécseli H L and Rasmussen J J 1991 *Phys. Fluids* B **3** 1609
[56] Takens F 1980 *Dynamical Systems and Turbulence (Warwick 1980) (Springer Lecture Notes in Mathematics vol 898)* ed D A Rand and L-S Young (Berlin: Springer) pp 366–81

[57] Kantz H and Schreiber T 1997 *Nonlinear Time Series Analysis (Cambridge Nonlinear Science Series vol 7)* (Cambridge: Cambridge University Press)
[58] Eckmann J-P 1981 *Rev. Mod. Phys.* **53** 643
[59] Swinney H L 1983 *Physica* D **7** 3
[60] Biskamp D and Kaifen H 1985 *Phys. Fluids* **28** 2172
[61] Klinger T, Latten A, Piel A, Bonhomme G, Pierre T and de Wit T D 1997 *Phys. Rev. Lett.* **79** 3913
[62] Hai F and Wong A Y 1970 *Phys. Fluids* **13** 672
[63] Bergé P, Pomeau Y and Vidal C 1984 *Order Within Chaos* (New York: Wiley)
[64] Grulke O, Greiner F, Klinger T and Piel A 2001 *Plasma Phys. Controlled Fusion* **43** 525
[65] Grulke O, Klinger T, Endler M, Piel A and the W7-AS team 2001 *Phys. Plasmas* **8** 5171
[66] Gravier E, Caron X, Bonhomme G and Pierre T 1999 *Phys. Plasmas* **6** 1670
[67] Shinbrot T 1995 *Adv. Phys.* **44** 73
[68] Schröder C, Klinger T, Block D, Piel A, Bonhomme G and Naulin V 2001 *Phys. Rev. Lett.* **86** 5711
[69] Naulin V 2002 *New J. Phys.* **4** 28